Freestream-turbulence decay and the sphere drag crisis predicted by the Langtry–Menter transition model

Yueqian Jiang

Independent Researcher, Beijing, China

ORCID: 0009-0005-9655-305X

yueqianleojiang@outlook.com

Abstract

Reynolds-averaged Navier–Stokes prediction of the drag crisis of bluff bodies, such as sports balls and a swimmer's head, requires a transition model whose predictions depend on the freestream turbulence intensity. However, two-equation models dissipate this turbulence before it reaches the body, and the consequence for the predicted crisis has not been quantified. This study mapped the drag crisis predicted by the Langtry–Menter transition model for a smooth sphere using 70 steady axisymmetric computations at Reynolds numbers of 1×10^5–1.14×10^6, with three inlet intensities and freestream decay uncontrolled or suppressed by sustaining terms. The computations were verified on three grids and validated against measurements. Uncontrolled decay lowered the intensity at the body increasingly with Reynolds number. The predicted crisis Reynolds number collapsed to within 7 % onto a single power law of the intensity at the body, for both decay treatments. At the experimental intensity, the predicted crisis Reynolds number was 26–60 % below the measured one: the drag fell before a separation bubble formed, and the steady wake recovered too much base pressure. Hence, the intensity reaching the body, not the inlet value, governs transition-model predictions near the drag crisis and should be controlled or reported.

Keywords: drag crisis; sphere; laminar–turbulent transition; Langtry–Menter model; freestream turbulence; decay control; Reynolds-averaged Navier–Stokes; verification and validation

1. Introduction

The drag of a smooth sphere falls abruptly over a narrow Reynolds number range. Below this range, the laminar boundary layer separates ahead of the equator, and the wake is wide; within it, the separated shear layer becomes turbulent, reattaches to form a separation bubble, and separates again farther downstream; consequently, the drag coefficient falls from approximately 0.5 to below 0.1. Achenbach [1] measured this drag crisis at a turbulence level of approximately 0.45 % and placed the critical Reynolds number, at which the drag coefficient reaches its minimum, near 3.7×10^5. The critical Reynolds num-

ber depends on the turbulence of the incident stream: Dryden et al. [2] used this dependence to characterize wind-tunnel turbulence, and Son et al. [3] found that freestream turbulence triggered a separation bubble and lowered the critical Reynolds number as its intensity increased.

Predicting the crisis numerically is correspondingly difficult because the result hinges on where the boundary layer becomes turbulent. Constantinescu and Squires [4] obtained improved predictions of the supercritical skin friction using detached-eddy simulation only after fixing the transition location at its measured position. Stabnikov et al. [5] needed very fine grids to predict the critical Reynolds number with a scale-resolving method. Fully turbulent Reynolds-averaged Navier–Stokes (RANS) models cannot represent the laminar boundary layer; Rosetti et al. [6] assessed the resulting modeling errors for a circular cylinder up to $Re = 5 \times 10^5$. Correlation-based transition models, such as the γ–$Re_{\theta t}$ model of Langtry and Menter [7, 8], make the predicted transition respond to the local turbulence intensity. Nakhostin and Giljarhus [9] applied this model to a sphere using steady RANS and obtained an improved subcritical drag but found the implementation unstable in the critical and supercritical ranges.

This sensitivity to the turbulence intensity creates a specific problem. Two-equation models dissipate freestream turbulence excessively between the inlet and the body [10, 11]; therefore, the intensity that reaches the boundary layer depends on the inlet distance, inlet eddy-viscosity ratio, and turbulence model, not only on the specified value. Spalart and Rumsey [10] proposed sustaining terms that hold the ambient turbulence at its inflow value. Lopes et al. [11] modified the freestream dissipation for the same purpose and demonstrated the technique on a flat plate, an airfoil, and a prolate spheroid. To the best of current knowledge, neither remedy has been applied to the sphere drag crisis, although the experimental critical Reynolds number itself depends on the freestream turbulence.

A previous three-dimensional unsteady RANS study of a swimmer's head modeled as a sphere [12] used the Langtry–Menter model at $Re = 3.2$–4.4×10^5. Its drag coefficient was approximately one-third of Achenbach's measured value at the lowest Reynolds number and approximately twice the measured value at the highest Reynolds number. The inlet turbulence intensity of 1 % decayed to 0.593 % at the body. A sensitivity test at a single Reynolds number showed that the drag depended strongly on the turbulence boundary condition. However, each three-dimensional unsteady run took several days; a systematic sweep over turbulence conditions and Reynolds numbers was therefore not feasible, and that study could not establish how the predicted crisis responded to freestream turbulence.

The present study maps that response using steady axisymmetric RANS computations of the same sphere, domain, fluid, turbulence model, and boundary conditions as [12]. It extends [12] in three respects: the inlet intensity and decay treatment are varied systematically over a decade of Reynolds number, from 1×10^5 to 1×10^6; controlled and uncontrolled decay, the latter as in [12], are compared to separate the specified intensity from the intensity that reaches the body; and the drag is related to the boundary-layer regime of every run. The objectives are to determine how the predicted crisis Reynolds

number depends on the specified intensity and the intensity at the body, whether uncontrolled decay acts only by lowering that intensity, and whether the model reproduces the laminar separation, separation bubble, and turbulent separation that Achenbach inferred. No previous study appears to have mapped the transition-model drag crisis of a sphere against freestream turbulence with decay both controlled and uncontrolled. Section 2 states the governing equations and the model, Section 3 the numerical method, and Section 4 the computational setup and grid study; Section 5 verifies and validates the computations, Section 6 defines the cases, Section 7 presents and discusses the results, and Section 8 concludes.

2. Governing equations and physical model

2.1 Conservation equations

The flow was treated as incompressible, steady in the Reynolds-averaged sense, and axisymmetric. In index notation, with mean velocity U_i, mean pressure p, density ρ, kinematic viscosity ν, and eddy viscosity ν_t, the RANS equations for mass and momentum read

$$\partial_j U_j = 0, \tag{1}$$

$$U_j \partial_j U_i = -\partial_i p/\rho + \partial_j[(\nu + \nu_t)(\partial_j U_i + \partial_i U_j)], \tag{2}$$

where ∂_j denotes differentiation with respect to the coordinate x_j, and the isotropic part of the Reynolds stress is absorbed in p.

2.2 Turbulence and transition model

The eddy viscosity was obtained from the k–ω shear-stress transport (SST) model [13], which solves for the turbulence kinetic energy k and the specific dissipation rate ω, coupled to the Langtry–Menter γ–$Re_{\theta t}$ transition model [7, 8] as implemented in OpenFOAM v2512 (kOmegaSSTLM) [14]:

$$U_j \partial_j k = \gamma_{\text{eff}} P_k - D_k + \partial_j[(\nu + \sigma_k \nu_t)\partial_j k] + \beta^* \omega_\infty k_\infty, \tag{3}$$

$$U_j \partial_j \omega = \alpha P_k/\nu_t - \beta\omega^2 + \partial_j[(\nu + \sigma_\omega \nu_t)\partial_j \omega] + C_{k\omega} + \beta\omega_\infty{}^2, \tag{4}$$

$$U_j \partial_j \gamma = P_\gamma - E_\gamma + \partial_j[(\nu + \nu_t/\sigma_f)\partial_j \gamma], \tag{5}$$

$$U_j \partial_j Re_{\theta t} = P_{\theta t} + \partial_j[\sigma_{\theta t}(\nu + \nu_t)\partial_j Re_{\theta t}]. \tag{6}$$

Here, P_k is the production of k; the dissipation $D_k = \gamma_d \beta^* k\omega$ is limited through γ_d, which is the effective intermittency γ_{eff} clipped to the range 0.1–1; and $C_{k\omega}$ is the SST cross-diffusion term. The blending functions, the source terms P_γ, E_γ, and $P_{\theta t}$, and the model coefficients are those of [7, 8, 13], at their default values. Transition onset depends on the local turbulence intensity through the correlation for the

transition-onset momentum-thickness Reynolds number, which in the freestream, at zero pressure gradient and for $Tu \leq 1.3$ (in percent), reads [7]

$$Re_{\theta t} = 1173.51 - 589.428\, Tu + 0.2196\, Tu^{-2}. \tag{7}$$

2.3 Freestream decay

Without the last terms of Eqs. (3) and (4), the freestream turbulence decays between the inlet and body. With k_∞ and ω_∞ set to the inlet values, the sustaining terms of Spalart and Rumsey [10] balance the freestream dissipation exactly and keep k and ω at their inflow values away from the body. Two treatments were compared: uncontrolled decay, with $k_\infty = \omega_\infty = 0$ as in [12], and controlled decay, with the sustaining terms enabled.

2.4 Assumptions and non-dimensional parameters

The sphere was smooth and fixed, and the fluid was water with $\nu = 1.0 \times 10^{-6}\ \mathrm{m^2\ s^{-1}}$ and $\rho = 998\ \mathrm{kg\ m^{-3}}$. The steady axisymmetric formulation excludes vortex shedding and other three-dimensional wake dynamics. The governing parameters were the Reynolds number $Re = U_\infty D/\nu$, with freestream speed U_∞ and diameter D; the turbulence intensity $Tu = (2k/3)^{1/2}/U_\infty$, specified at the inlet as Tu_{in} and evaluated at the body as Tu_{body}; and the inlet eddy-viscosity ratio ν_t/ν. The drag coefficient is $C_d = F_x/(0.5\,\rho U_\infty{}^2\, A)$, where F_x is the streamwise force and A the frontal area, and the pressure coefficient is $C_p = (p - p_\infty)/(0.5\,\rho U_\infty{}^2)$, where p_∞ is the freestream pressure.

3. Numerical methodology

The equations were discretized using the cell-centered finite-volume method of OpenFOAM v2512 [14] (build _87ed40d2-20251219, the same as in [12]) and solved using the steady SIMPLEC pressure–velocity algorithm (simpleFoam). Convection of momentum used the bounded second-order linear-upwind scheme and convection of k, ω, γ, and $Re_{\theta t}$ the bounded first-order upwind scheme, as in [12]. Gradients, diffusion terms, and face interpolation used second-order central differencing, with a cell limiter on the velocity gradient. Pressure was solved using a geometric–algebraic multigrid solver, and the other variables were solved using a symmetric Gauss–Seidel smoother. The under-relaxation factors were 0.9 for momentum and 0.7 for the turbulence and transition variables; pressure, consistent with SIMPLEC, was not under-relaxed. Because the computations were steady, no temporal discretization was used; the solution advanced through under-relaxed SIMPLEC iterations from a uniform initial field.

A run was stopped when two conditions were met: the mean drag coefficient over the last 2000 iterations differed from the mean over the preceding 2000 by less than 0.1 %, and the root-mean-square fluctuation

of the drag coefficient over the last 2000 iterations was below 0.5 % of its mean. Every run had a minimum of 6000 iterations and an iteration limit of 20,000 or 30,000.

4. Computational setup

4.1 Geometry and computational domain

The sphere of [12] had a diameter $D = 0.2\,\mathrm{m}$, and Re was set through the freestream speed $U_\infty = 0.5\text{–}5.7\,\mathrm{m\,s^{-1}}$. The domain was a 5° wedge about the streamwise axis, one cell thick, extending 5D upstream, 15D downstream, and 5D from the axis (Fig. 1), the same distances as in the three-dimensional domain of [12]. The blockage ratio was 1.0 %.

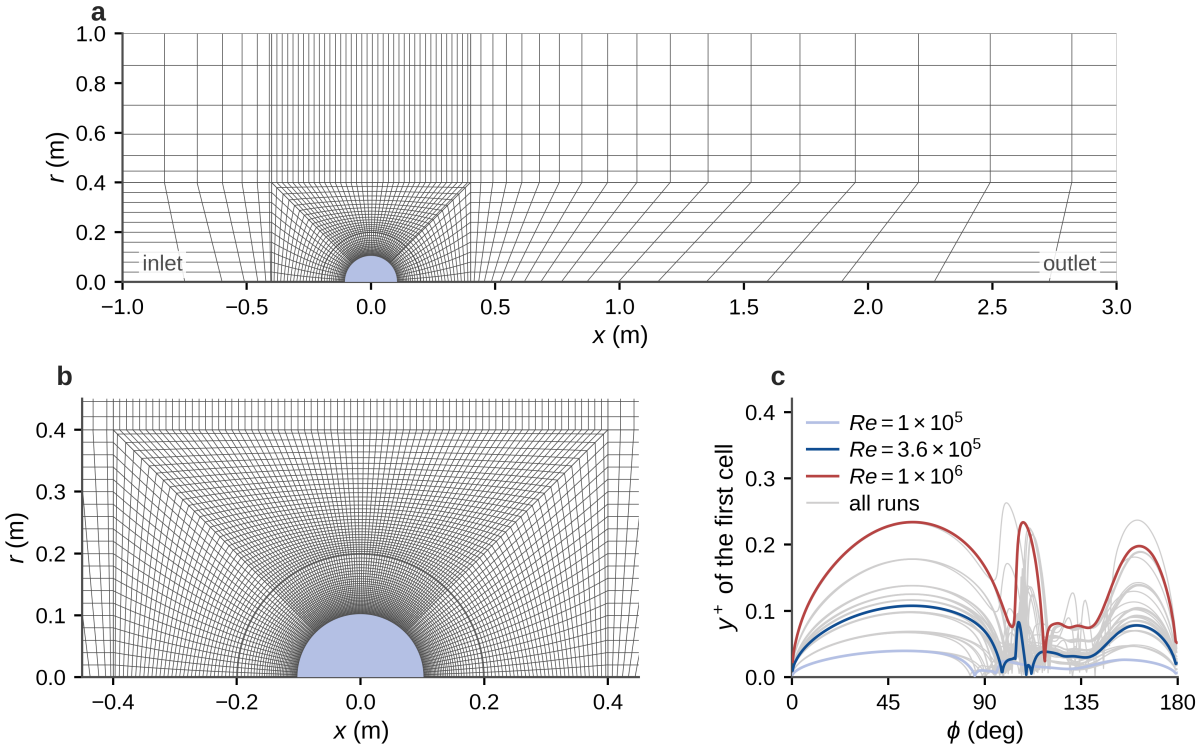


Fig. 1 *Computational domain and production mesh. (a) The entire domain in the meridional plane, with every eighth grid line drawn. (b) The O-grid and the surrounding blocks, with every fourth grid line drawn. (c) Wall distance of the first cell center in wall units, y^+, along the surface; colored lines, $Tu_{in} = 0.45$ % with controlled decay; gray lines, the other runs of the production matrix*

4.2 Grid generation and refinement strategy

The block-structured grid was generated by a script that writes the blockMesh dictionary from a few parameters. An O-grid ring extended from the sphere to a radius of 1D, a second ring to a square of half-width 2D, and H-blocks to the domain boundaries. The resolution was concentrated in the regions with the steepest gradients: wall-normally, the first cell was 2 µm high and grew at a ratio of 1.10 over 54

cells, which spanned the first 3.4 mm and contained the boundary layer, and at 1.012 beyond; along the surface, 460 cells were spaced at 0.3° (0.52 mm) between 45° and 135° from the front stagnation point, the band in which transition and separation occurred, and at 0.56° elsewhere. The grading was continuous across block faces. The production grid had 176,630 cells, a maximum non-orthogonality of 44.8°, and a maximum skewness of 0.77.

4.3 Boundary and initial conditions

The boundary conditions were those of [12]. The inlet had a uniform velocity and fixed values of $k = 1.5\,(Tu_{\mathrm{in}}\,U_\infty)^2$, ω from an eddy-viscosity ratio of 10, $\gamma = 1$, and $Re_{\theta t}$ from Eq. (7); the outlet had a fixed static pressure and inlet–outlet conditions on the other variables; the lateral boundary was a slip wall; and the sphere was a smooth no-slip wall with low-Reynolds-number wall conditions for k, ω, and ν_t, appropriate at $y^+ < 1$, and zero normal gradient of γ and $Re_{\theta t}$. The two side planes were wedge (axisymmetric) boundaries. The initial field was uniform at the inlet values.

4.4 Mesh independence

Coarse and fine grids were generated using the same script, with every cell count multiplied by $2^{-1/2}$ and $2^{1/2}$, respectively, and the first-cell height scaled accordingly (91,408 and 341,899 cells; refinement ratio $2^{1/2}$ in each direction). All three grids were run at $Re = 3.6 \times 10^5$, in the separation-bubble regime, and at 1×10^6, where the wall shear was highest, both at $Tu_{\mathrm{in}} = 0.45$ % with controlled decay. The refinement was systematic rather than adaptive, because the grid convergence index [15] requires geometrically similar grids; the grid was instead adapted a priori by concentrating cells in the boundary-layer band (Section 4.2). Table 1 lists the results. The drag coefficient converged monotonically, with observed orders of 1.6 and 1.3 and fine-grid convergence indices [15] of 7.4 and 6.2 %; the production-grid values were 4.4 and 2.8 % above the fine-grid values. The production-grid separation angle was within 0.3 % of the fine-grid value. The transition-onset angle, a threshold quantity, converged less well: at 3.6×10^5, the medium and fine grids agreed to within 0.5°, but at 1×10^6, it varied non-monotonically between 94° and 102° across the three grids. The coarse grid did not resolve the separation bubble at 3.6×10^5, whereas the medium and fine grids captured it, with reattachment at 109.4° and 109.8°; the medium grid was therefore used for production. Fine-grid repeats at $Re = 3.6 \times 10^5$ for $Tu_{\mathrm{in}} = 0.2$ and 1 % with controlled decay and for 1 % with uncontrolled decay confirmed that the intensity effect was not a grid artifact. The production-grid drag coefficients were between 0.7 % below and 5.8 % above the fine-grid values, the regimes and Tu_{body} were unchanged, and the separation angle changed by at most 0.4°; the drag coefficient at 0.2 % exceeded that at 0.45 % by 31 % on the production grid and by 37 % on the fine grid.

Table 1 Grid study at Tu_{in} = 0.45 % with controlled decay. C_d is the drag coefficient and φ_s the separation angle; the observed order of accuracy is p, and GCI is the fine-grid convergence index [15]

Re	Quantity	Coarse	Medium	Fine	*p*	GCI
3.6×10^5	C_d	0.1162	0.1083	0.1038	1.6	7.4 %
3.6×10^5	φ_s (deg)	97.7	98.1	98.3	2.3	0.2 %
1×10^6	C_d	0.0760	0.0729	0.0709	1.3	6.2 %
1×10^6	φ_s (deg)	117.4	118.0	118.2	1.7	0.4 %

5. Verification and validation

5.1 Iterative convergence

All runs met the convergence criterion of Section 3 after 6013–22,773 iterations; the largest root-mean-square fluctuation of the drag coefficient over the final window was 0.40 % of its mean, and the largest drift between successive windows was below 0.1 %. The maximum y^+ of the first cell on the sphere was 0.28 on the production grid (Fig. 1c) and 0.33 on the coarse grid, well below the limit of $y^+ \approx 1$ that the model requires for wall resolution.

5.2 Code and solution verification

The solver and the turbulence and transition models were those of a widely used open-source release [14]; the present work therefore checked the implementation against one exact solution and verified the solutions themselves. As the benchmark, the freestream decay was compared with the solution of the k–ω equations for decaying turbulence in uniform flow, $k = k_0(1 + \beta\omega_0\, t)^{-\beta^*/\beta}$ and $\omega = \omega_0/(1 + \beta\omega_0\, t)$, with $\beta = 0.0828$, $\beta^* = 0.09$, and the convective time t. Over the first $2.5D$ downstream of the inlet, where the velocity differed from U_∞ by less than 1 %, the computed k of all 27 production runs with uncontrolled decay followed this solution to within 7 %, and the intensity to within 3.6 %; the deviation grew with the amount of decay, consistent with the first-order convection of k and ω. With controlled decay, the intensity remained at its inlet value, as the sustaining terms require. The observed orders of accuracy of the drag coefficient, 1.3–1.6 (Table 1), lie between the first-order convection of the turbulence variables and the second-order discretization of the remaining terms, as expected. The resulting discretization uncertainty of 6–7 % in the drag coefficient is expected to be largely systematic across the cases, because all the cases used the same grid. It is smaller than the effects reported in Section 7, which reach a factor of two.

5.3 Validation

Three comparisons assessed the computations against reference results. First, the freestream decay reproduced the three-dimensional computation of [12] under the conditions of that study ($Re = 3.6 \times 10^5$, $Tu_{in} = 1$ %, uncontrolled decay; Fig. 2): at 0.90, 0.41, and 0.13 m upstream of the stagnation point, the intensity was 0.990, 0.675, and 0.587 %, against 1.000, 0.672, and 0.593 % in [12].

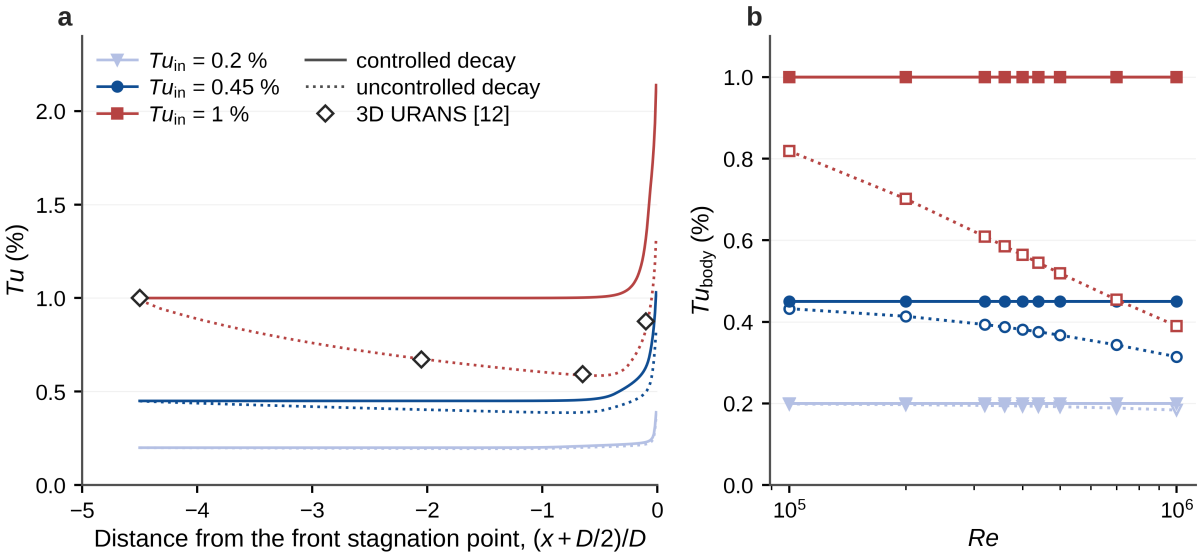


Fig. 2 *Freestream turbulence intensity. (a) Along the stagnation streamline at $Re = 3.6 \times 10^5$; solid lines, controlled decay; dotted lines, uncontrolled decay; diamonds, the three-dimensional computation of [12] at $Tu_{in} = 1$ % with uncontrolled decay. (b) Intensity reaching the body against Reynolds number; filled symbols, controlled decay; open symbols, uncontrolled decay*

Second, the computed forebody pressure agreed with Achenbach's surface-pressure measurements [1] at $Re = 1.62 \times 10^5$, 3.18×10^5, and 1.14×10^6 (Fig. 3) to within approximately 0.1 in C_p up to 45° at all three Reynolds numbers and up to 70° at the two higher ones. The suction peak was too deep at 1.62×10^5 (−0.85 against −0.53) and close to the measurements at the higher Reynolds numbers (−1.05 and −1.14 against −0.98 and −1.11). Downstream of the separation point, the computed pressure recovered too much: the base pressure coefficient, averaged over $\varphi > 170°$, was −0.05, 0.05, and 0.15, against −0.27, −0.13, and −0.02.

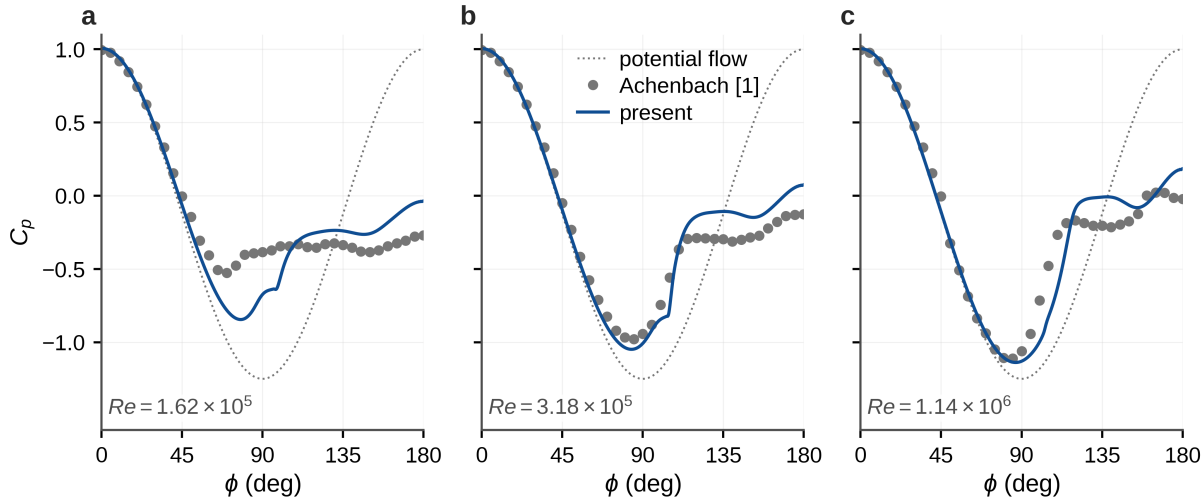


Fig. 3 *Surface pressure coefficient at the Reynolds numbers of Achenbach's measurements [1], Tu_{in} = 0.45 % with controlled decay. Dotted line, potential flow*

Third, the laminar separation angle at Tu_{in} = 0.45 % was 88.8° at $Re = 1.62 \times 10^5$ and 95° at 2.8×10^5 (interpolated), against 82° and 95° reported by Achenbach [1]. Pressure drag accounted for 87–98 % of the total drag in all runs, consistent with his finding that friction contributed at most 12.5 %. Therefore, the computations reproduced the forebody pressure and, to within 7°, the laminar separation angle, whereas the base pressure was too high. Section 7 returns to this difference.

6. Case studies

The production matrix combined nine Reynolds numbers, Re = 1.0, 2.0, 3.2, 3.6, 4.0, 4.4, 5.0, 7.0, and 10×10^5; three inlet intensities, Tu_{in} = 0.2, 0.45, and 1.0 %; and both decay treatments, resulting in 54 runs. The Reynolds number range spanned the subcritical, critical, and supercritical regimes of Achenbach's measurements [1] and included the four Reynolds numbers of [12]. The intensities bracketed Achenbach's 0.45 %, from a quieter stream to the 1 % of [12]. Three further runs, at the Reynolds numbers of Achenbach's pressure distributions, were used for the validation in Section 5.3; four were used for the grid study; and six were used to test the inlet eddy-viscosity ratio, which was raised from 10 to 50 at Tu_{in} = 0.45 % and Re = 2.0, 3.6, and 7.0×10^5 with both decay treatments. With the three fine-grid repeats, the study comprised 70 simulations.

The following quantities were evaluated in every run. The intensity at the body, Tu_{body}, was the minimum of Tu on the stagnation streamline upstream of $x = -0.105$ m, excluding the amplification in the stagnation region [12]. The separation angle φ_s, measured from the front stagnation point, was the first angle at which the meridional wall shear stress reversed direction and remained reversed [12]; a reattachment within 20° of it, at φ_r, marked a separation bubble, followed by the final separation at φ_{s2}. Transition onset φ_t was the first angle past the intermittency minimum at which γ, sampled 0.1 mm from

the wall, reached 0.5; a rise downstream of the final separation lay in the wake and was not counted. Each run was classified as laminar separation, separation bubble, or turbulent separation, the last when transition onset preceded the first separation. Because the computed drag curves had no minimum within the simulated range, the crisis was located by $Re_{0.2}$, the Reynolds number at which the drag coefficient fell through 0.2; this crossing was interpolated linearly in the logarithm of Re. The level of 0.2 lies within Achenbach's steep drop from 0.51 to 0.06, which passed through it at $Re = 3.57 \times 10^5$.

7. Results and discussion

7.1 Turbulence reaching the body

In every run, controlled decay held the freestream intensity at its inlet value up to the stagnation region. With uncontrolled decay, the intensity at the body was lower than that at the inlet and fell further as the Reynolds number increased (Fig. 2b): for $Tu_{in} = 1$ %, from 0.82 % at $Re = 1 \times 10^5$ to 0.39 % at 1×10^6, and for 0.45 %, from 0.43 to 0.31 %; at 0.2 %, the decay was below 0.02 percentage points. The Reynolds number dependence arose from the inlet condition: at a fixed eddy-viscosity ratio, ω, and with it the specific decay rate $\beta^* \omega$ of k, scales with U_∞^2, whereas the convective time to the body decreases only as $1/U_\infty$; consequently, the decay accumulated upstream of the body grows with U_∞.

7.2 Flow field

The flow fields at $Tu_{in} = 0.45$ % illustrate the three regimes (Fig. 4). At $Re = 1 \times 10^5$, the laminar boundary layer separated at 85°, and the separated shear layer bounded a recirculation region extending $1.04D$ behind the rear of the sphere. At 3.6×10^5, the boundary layer separated while still laminar at 98°, the intermittency rose in the separated shear layer, and the flow reattached at 109° before separating again at 112°; the recirculation region shortened to $0.65D$. At 1×10^6, the intermittency rose within the attached boundary layer from 88° and reached 0.5 near the wall at 102°, and the turbulent boundary layer separated at 118° without a bubble, leaving a recirculation region of $0.56D$.

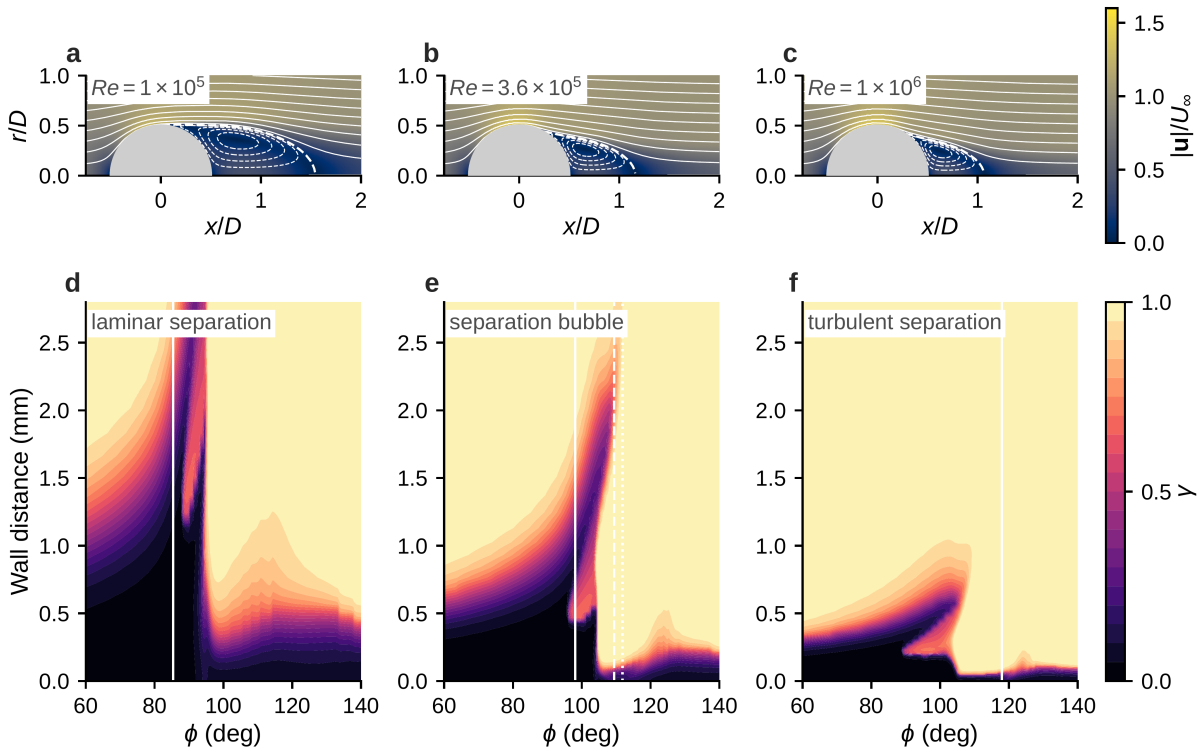


Fig. 4 *Flow field at Tu_{in} = 0.45 % with controlled decay at Re = 1 × 10^5^, 3.6 × 10^5^, and 1 × 10^6^. (a–c) Velocity magnitude and streamlines in the meridional plane, with the flow from left to right; the streamlines are contours of the Stokes stream function, dashed inside the recirculation region, and the thick dashed line is the dividing streamline. (d–f) Intermittency in the boundary layer, against the angle from the front stagnation point and the wall distance; solid lines, first separation; dashed line, reattachment; dotted line, final separation*

7.3 Drag coefficient

The computed drag coefficient decreased continuously over the entire Reynolds number range instead of dropping abruptly as it did in the experiment (Fig. 5). At $Re = 1 \times 10^5$, it was 0.35 at $Tu_{\mathrm{in}} = 0.2$ % and 0.22–0.25 at 1 %, well below Achenbach's subcritical 0.51, and at 1×10^6, it was 0.055–0.073 against 0.11. The freestream turbulence mattered most at low Reynolds numbers: at $Re = 2 \times 10^5$, raising Tu_{in} from 0.2 to 1 % halved the drag coefficient, from 0.27 to 0.14–0.15. The decay treatment mattered only where it changed Tu_{body} appreciably: at 0.2 %, the drag coefficients of the two treatments agreed to within 2 %, whereas at 1 % and $Re = 4.4 \times 10^5$, controlled decay gave 0.117 and uncontrolled decay 0.100. At the conditions of [12], the axisymmetric drag coefficients were 18–26 % below the three-dimensional values.

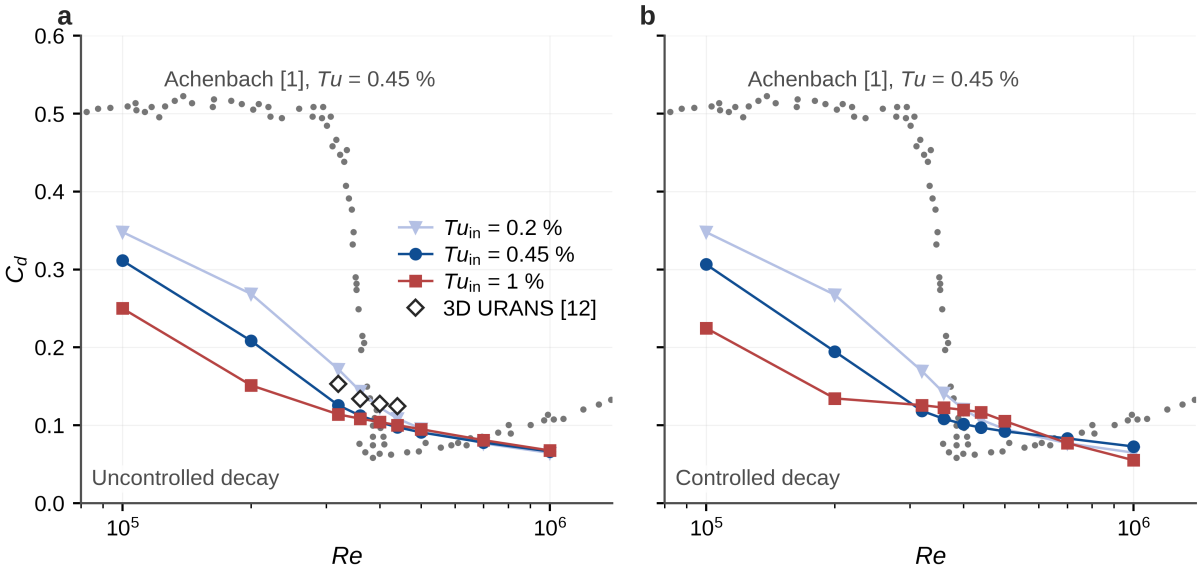


Fig. 5 *Drag coefficient against Reynolds number for the three inlet intensities, with (a) uncontrolled and (b) controlled decay. Gray dots, the measurements of Achenbach [1]; diamonds, the three-dimensional unsteady computation of [12] at Tu_{in} = 1 % with uncontrolled decay*

7.4 Crisis Reynolds number

With controlled decay, the computed $Re_{0.2}$ decreased from 2.8×10^5 at Tu_{in} = 0.2 % to 1.2×10^5 at 1 % (Table 2). At Achenbach's intensity of 0.45 %, controlled decay gave $Re_{0.2} = 1.94 \times 10^5$, 46 % below the measured value. Uncontrolled decay raised $Re_{0.2}$ by 8 % at Tu_{in} = 0.45 % and by 17 % at 1 %. When plotted against the intensity that reached the body, the six series collapsed onto one curve (Fig. 6), $Re_{0.2} \approx 1.25 \times 10^5\ Tu_{body}^{-0.51}$, with Tu_{body} in percent and a maximum deviation of 6.8 %. Therefore, uncontrolled decay shifted the predicted crisis mainly by lowering Tu_{body}.

Table 2 Crisis Reynolds number $Re_{0.2}$, at which the drag coefficient C_d falls through 0.2, and C_d for each series. Tu_{body} is the intensity at the body at $Re_{0.2}$; the bubble column lists the lowest simulated Reynolds number with a separation bubble. Achenbach's values are from his drag curve [1]

Tu_{in} (%)	Decay	Tu_{body} (%)	$Re_{0.2}$ ($\times 10^5$)	Bubble from Re ($\times 10^5$)	C_d at $Re = 10^5$	C_d at $Re = 10^6$
0.2	Uncontrolled	0.196	2.79	5.0	0.348	0.065
0.2	Controlled	0.200	2.77	5.0	0.348	0.065
0.45	Uncontrolled	0.412	2.10	4.0	0.311	0.066
0.45	Controlled	0.450	1.94	3.6	0.306	0.073
1.0	Uncontrolled	0.759	1.42	3.6	0.250	0.068
1.0	Controlled	1.000	1.21	3.2	0.225	0.055
Achenbach [1]	–	0.45	3.57	–	0.51	0.11

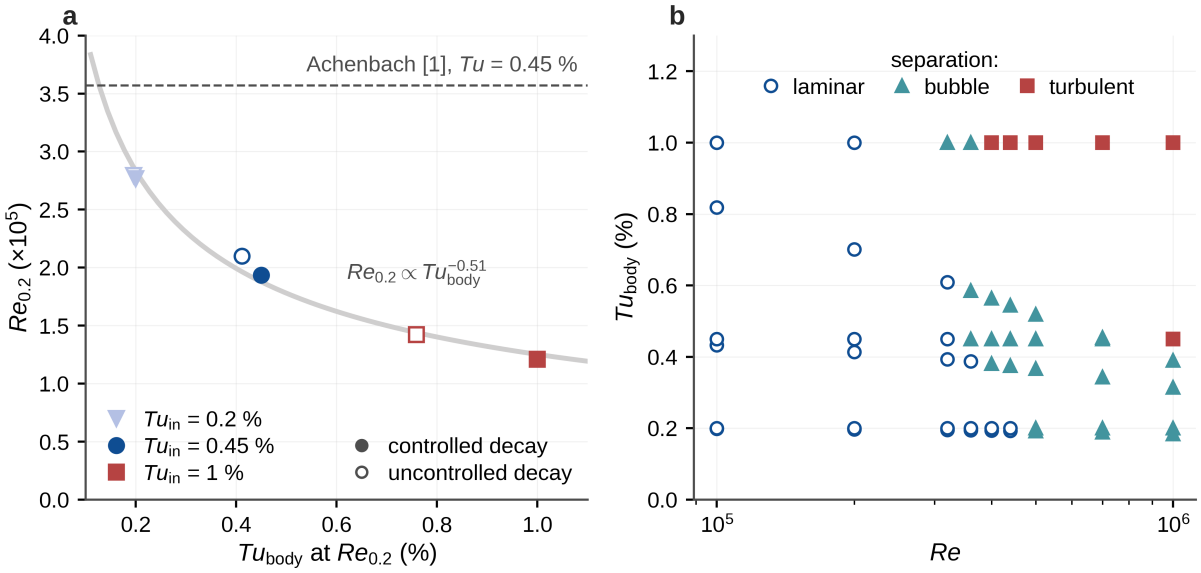


Fig. 6 *(a) Crisis Reynolds number $Re_{0.2}$ against intensity at the body at that Reynolds number; filled symbols, controlled decay; open symbols, uncontrolled decay; gray line, power-law fit; dashed line, crisis Reynolds number measured by Achenbach [1] at Tu = 0.45 %. (b) Boundary-layer regime of every production run against Reynolds number and the intensity at the body*

Because the computed drop was gradual and the measured one abrupt, the size of the discrepancy depends on the drag level used to locate the crisis: thresholds of 0.15 and 0.25 gave discrepancies of 26 and 60 %, respectively, instead of 46 %, relative to Achenbach's crossings at 3.58 and 3.56 × 10^5. The collapse itself held for both thresholds, with exponents of −0.42 and −0.54 and maximum deviations of at most 5 %. According to the fit for the 0.2 level, $Re_{0.2}$ would reach Achenbach's value only at $Tu_{body} \approx 0.13$ %, less than one-third of his measured intensity.

7.5 Boundary-layer regimes

As the Reynolds number increased, every series moved from laminar separation to a separation bubble, and the controlled series at Tu_{in} = 0.45 and 1 % then reached turbulent separation, the third regime that Achenbach inferred (Fig. 6b); a higher Tu_{body} moved each regime boundary to lower Reynolds numbers. The bubble appeared at $Re = 5 \times 10^5$ for Tu_{in} = 0.2 %, at 3.6–4.0 × 10^5 for 0.45 %, and at 3.2–3.6 × 10^5 for 1 %; turbulent separation without a bubble occurred only with controlled decay, from $Re = 4 \times 10^5$ at 1 % and at 1 × 10^6 at 0.45 %. At 0.45 %, the laminar separation angle increased from 85° at $Re = 1 \times 10^5$ to 97° at 3.2 × 10^5 (Fig. 7). In the bubble regime, the boundary layer separated at 98–102°, transition onset in the separated shear layer occurred at 104–107°, the flow reattached at 106–110°, and the final separation followed at 112–120°.

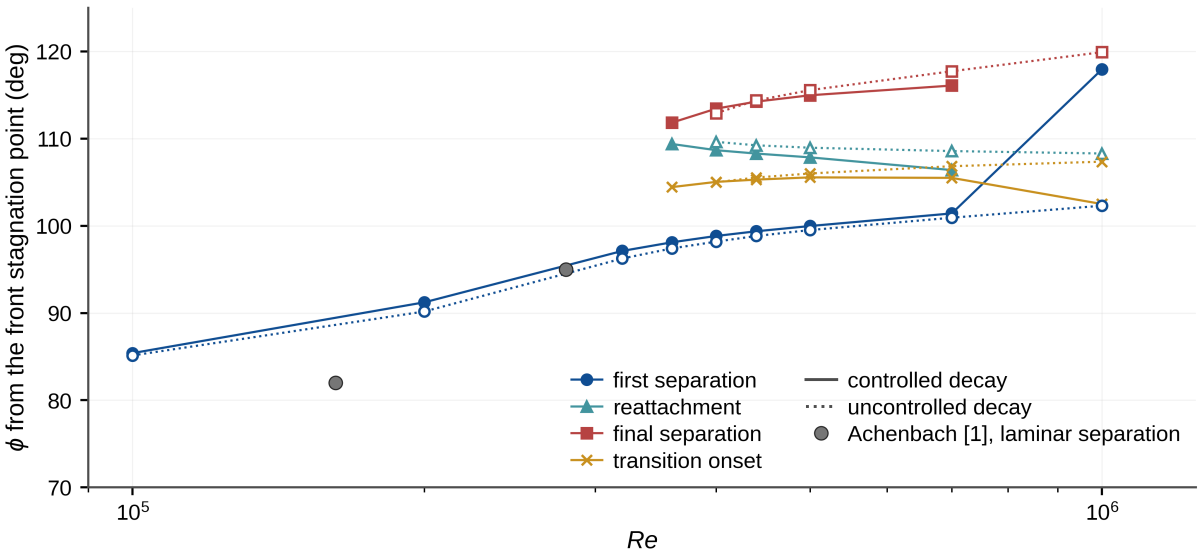


Fig. 7 *First separation, reattachment, final separation, and transition onset at Tu_{in} = 0.45 %; reattachment and final separation are shown where a separation bubble formed. Gray circles, laminar separation reported by Achenbach [1]*

The drag did not track the boundary-layer regime. At Tu_{in} = 0.45 % with controlled decay, the drag coefficient had already fallen to 0.2 by $Re = 1.9 \times 10^5$, while laminar separation persisted; the bubble appeared only at 3.6×10^5, where the drag coefficient was already 0.11. At 1 % and $Re = 4.4 \times 10^5$, the controlled run, in which the turbulent boundary layer separated at 107° without a bubble, had a higher drag coefficient (0.117) than the uncontrolled run (0.100), in which a bubble formed and the final separation occurred at 113°.

7.6 Sensitivity to the inlet eddy-viscosity ratio

Raising the inlet eddy-viscosity ratio from 10 to 50 at Tu_{in} = 0.45 % and $Re = 2.0$, 3.6, and 7.0×10^5 changed the drag coefficient by −5.4 to +9.3 % with controlled decay and by +0.3 to +3.3 % with uncontrolled decay. With uncontrolled decay, part of the change came from the slower decay at the higher ratio, which raised Tu_{body} from 0.34–0.41 to 0.42–0.44 %. Interpolated between $Re = 2.0$ and 3.6×10^5, $Re_{0.2}$ rose by approximately 11 % with controlled decay and by 4 % with uncontrolled decay. At 3.6×10^5 with controlled decay, the separation bubble did not form at the higher ratio; therefore, the regime boundary near this Reynolds number also depended on the freestream turbulence length scale, which the eddy-viscosity ratio sets. These changes were secondary to the effect of the intensity, which changed $Re_{0.2}$ by more than a factor of two, and smaller than the 19 % drag change found in three dimensions [12]; they nevertheless show that the intensity alone does not fully specify the freestream turbulence.

7.7 Discussion

The first finding concerns practice. In this model, the predicted drag crisis depends on the freestream turbulence mainly through the intensity that reaches the body, and with uncontrolled decay that intensity depends on the Reynolds number as well as on the inlet value. A drag curve computed at a fixed inlet intensity and eddy-viscosity ratio is therefore a curve along which the effective freestream turbulence varies; under the conditions of [12], for example, the intensity at the body in the present computations was 0.61 % at $Re = 3.2 \times 10^5$ and 0.54 % at 4.4×10^5. Controlled decay removes this dependence and makes the specified intensity the one the boundary layer receives. Whichever treatment is used, the intensity at the body is the quantity to report alongside transition-sensitive drag coefficients, consistent with the conclusion of [12] for the eddy-viscosity ratio.

The second finding is that matching the freestream intensity does not make the predicted crisis agree with the experiment. At Achenbach's intensity, the computed crisis occurred at a Reynolds number 26–60 % too low, and reproducing his crossing of 0.2 would require an intensity at the body less than one-third of the one he measured. The comparison assumes that his tunnel intensity corresponds to the model's Tu_{body}; his turbulence length scale was not reported, whereas in the model it is set by the eddy-viscosity ratio. The regime map indicates why the crisis occurred early: the computed drag fell while laminar separation persisted, as the separation angle moved downstream and the base pressure rose, whereas in the experiment the fall coincided with the formation of the separation bubble [1]. The validation of Section 5.3 locates the discrepancy behind separation, in a base pressure 0.17–0.22 too high, rather than in the attached boundary layer. A steady axisymmetric wake cannot shed or precess, and the axisymmetric drag coefficients were 18–26 % below those of the three-dimensional unsteady computation of [12] at the same conditions (Section 7.3); the excess pressure recovery is therefore attributed mainly to the missing wake dynamics.

These findings pertain to transition-sensitive simulations of bodies in this range, such as a swimmer's head at $Re = 3.2\text{–}4.4 \times 10^5$ [12]. In this range, the six turbulence conditions of this study altered the computed boundary-layer regime and varied the drag coefficient by a factor of 1.2–1.5; therefore, comparisons between geometries are meaningful only at the same intensity at the body, as in [12].

8. Conclusions

Steady axisymmetric RANS computations of a sphere using the Langtry–Menter transition model, over $Re = 1 \times 10^5\text{–}1 \times 10^6$ with three freestream intensities and with freestream decay controlled and uncontrolled, led to four findings.

1. With uncontrolled decay, the intensity reaching the body was lower than that specified and fell as the Reynolds number increased, from 0.82 to 0.39 % for an inlet intensity of 1 %; controlled decay held it at the inlet value.

2. The predicted crisis Reynolds number collapsed onto a single function of the intensity at the body, $Re_{0.2} \approx 1.25 \times 10^5\ Tu_{\mathrm{body}}{}^{-0.51}$, to within 7 %, regardless of the decay treatment.

3. At Achenbach's intensity, the predicted crisis occurred at a Reynolds number 26–60 % too low; the drag fell before a separation bubble formed, and the computed base pressure was 0.17–0.22 too high.

4. The model nevertheless reproduced the sequence of laminar separation, separation bubble, and turbulent separation, the last at the two higher intensities with controlled decay, and the regime boundaries moved to lower Reynolds numbers as the intensity at the body increased.

The study contributes a map of the transition-model drag crisis of a sphere against freestream turbulence with decay both controlled and uncontrolled. It extends earlier sphere computations with this model by covering a decade of Reynolds number, by separating the specified intensity from the intensity that reaches the body, and by relating the predicted drag to the boundary-layer regime of every run. In practice, the intensity at the body, rather than the inlet value, sets the predicted crisis; for transition-sensitive simulations near the drag crisis, it should be controlled or at least measured and reported. The quantitative crisis Reynolds numbers are specific to the Langtry–Menter model with default coefficients in steady axisymmetric flow; testing whether the early crisis persists in three-dimensional unsteady or scale-resolving simulations with controlled freestream turbulence is a natural next step.

9. References

[1] Achenbach E (1972) Experiments on the flow past spheres at very high Reynolds numbers. J Fluid Mech 54(3):565–575. https://doi.org/10.1017/S0022112072000874

[2] Dryden HL, Schubauer GB, Mock WC, Skramstad HK (1937) Measurements of intensity and scale of wind-tunnel turbulence and their relation to the critical Reynolds number of spheres. NACA Report 581. National Advisory Committee for Aeronautics, Washington, DC

[3] Son K, Choi J, Jeon W-P, Choi H (2010) Effect of free-stream turbulence on the flow over a sphere. Phys Fluids 22(4):045101. https://doi.org/10.1063/1.3371804

[4] Constantinescu G, Squires K (2004) Numerical investigations of flow over a sphere in the subcritical and supercritical regimes. Phys Fluids 16(5):1449–1466. https://doi.org/10.1063/1.1688325

[5] Stabnikov AS, Garbaruk AV, Strelets MKh (2024) Numerical simulation of the drag crisis on a sphere using a scale-resolving approach. Fluid Dyn 59(3):465–478. https://doi.org/10.1134/S0015462823603248

[6] Rosetti GF, Vaz G, Fujarra ALC (2012) URANS calculations for smooth circular cylinder flow in a wide range of Reynolds numbers: solution verification and validation. J Fluids Eng 134(12):121103. https://doi.org/10.1115/1.4007571

[7] Langtry RB, Menter FR (2009) Correlation-based transition modeling for unstructured parallelized computational fluid dynamics codes. AIAA J 47(12):2894–2906. https://doi.org/10.2514/1.42362

[8] Menter FR, Langtry RB, Likki SR, Suzen YB, Huang PG, Völker S (2006) A correlation-based transition model using local variables—Part I: Model formulation. J Turbomach 128(3):413–422. https://doi.org/10.1115/1.2184352

[9] Nakhostin SM, Giljarhus KET (2019) Investigation of transitional turbulence models for CFD simulation of the drag crisis for flow over a sphere. IOP Conf Ser Mater Sci Eng 700:012007. https://doi.org/10.1088/1757-899X/700/1/012007

[10] Spalart PR, Rumsey CL (2007) Effective inflow conditions for turbulence models in aerodynamic calculations. AIAA J 45(10):2544–2553. https://doi.org/10.2514/1.29373

[11] Lopes R, Eça L, Vaz G, Kerkvliet M (2022) A technique to control the decay of freestream turbulence for transitional flow simulations. AIAA J 60(6):3565–3580. https://doi.org/10.2514/1.J061266

[12] Jiang Y (2026) Surface texture, boundary-layer transition, and drag on a swimmer's head: a computational study across the sphere drag crisis. engrXiv. https://doi.org/10.31224/8528

[13] Menter FR (1994) Two-equation eddy-viscosity turbulence models for engineering applications. AIAA J 32(8):1598–1605. https://doi.org/10.2514/3.12149

[14] Weller HG, Tabor G, Jasak H, Fureby C (1998) A tensorial approach to computational continuum mechanics using object-oriented techniques. Comput Phys 12(6):620–631. https://doi.org/10.1063/1.168744

[15] Celik IB, Ghia U, Roache PJ, Freitas CJ, Coleman H, Raad PE (2008) Procedure for estimation and reporting of uncertainty due to discretization in CFD applications. J Fluids Eng 130(7):078001. https://doi.org/10.1115/1.2960953

[16] Jiang Y (2026) Freestream-turbulence decay and the sphere drag crisis predicted by the Langtry–Menter transition model: simulation data, analysis scripts, and meshes, version 1.0.0. Zenodo. https://doi.org/10.5281/zenodo.23526275

10. Acknowledgements

This work used OpenFOAM v2512, developed and released by OpenCFD Ltd (Keysight Technologies, Bracknell, UK).

CRediT author statement

Yueqian Jiang: Conceptualization, Methodology, Software, Validation, Formal analysis, Investigation, Data curation, Visualization, Writing – original draft, Writing – review and editing.

Funding

No funding was obtained for this work.

Disclosure statement

The author reports there are no competing interests to declare.

Declaration of generative AI use

During this study, the author used Claude Opus 5.5 (Anthropic, San Francisco, CA, USA) for language editing and clarity improvement of the manuscript. After using this tool, the author reviewed and edited the content as needed and takes full responsibility for the content of the publication.

Data availability

The data that support the findings of this study are openly available on Zenodo under the Creative Commons Attribution 4.0 International license. They comprise the case-generation, run-control, analysis, and figure scripts; the input dictionaries, final fields, function-object output, and solver logs of all 70 runs; and the three meshes. The record is available at https://doi.org/10.5281/zenodo.23526275 [16].